Supplementary Information for: ‘Capturing atomic wetting dynamics in real time’

George T. Tebbutt[1], Christopher S. Allen[1,2], Anna Fabijańska[3], Barbara M. Maciejewska[1], Nicole Grobert[1]*

[1]*Department of Materials, University of Oxford, Oxford, OX1 3PH, United Kingdom.*

[2]*Electron Physical Science Imaging Centre, Diamond Light Source, Harwell Science and Innovation Campus, Didcot, OX11 ODE, United Kingdom.*

[3]*Lodz University of Technology, Institute of Applied Computer Science, 18 Stefanowskiego Str., 90-537 Lodz, Poland.*

*nicole.grobert@materials.ox.ac.uk

Supplementary Contents:

1. Crystallisation and orientation analysis of encapsulated Sn nanowires

The interplanar d-spacings of encapsulated Sn nanowires were determined from Fast Fourier Transform (FFT) patterns obtained from atomic-resolution TEM (ARTEM) micrographs. These FFTs capture the spatial frequency of the periodic atomic lattice and correspond to the reciprocal lattice of the imaged zone axis. The spatial resolution was estimated from spot broadening of the FFT spots, yielding uncertainties of ± 0.35 nm^{-1} for the tetragonal reflections and ± 0.378 nm^{-1} and ± 0.326 nm^{-1} for cubic reflections. Comparison between the measured *d*-spacings and bulk β-Sn is presented in Supplementary Table S1 and Table S2 below for both the cubic and tetragonal phase, respectively. The reference reflection list was generated by modelling the β-Sn structure (space group $I4_1/amd$; a = 5.83 Å, c = 3.18 Å) in CrystalMaker and simulating the powder X-ray Diffraction (XRD) pattern to extract expected reflection positions and intensities. Minor deviations between measured and reference *d*-spacings may arise from local strain in the encapsulated Sn, projection effects, or imaging aberrations.

Table S1: Measured and reference interplanar spacings for encapsulated β-Sn nanowire viewed down the cubic [001] zone axis.

assigned plane	FFT freq. (nm^{-1})	FFT ± Δfreq. (nm^{-1})	measured d (Å)	± Δd (Å)	literature d (Å)	Δd (Å) = meas – lit	deviation (%)
(4 0 0)	6.819	0.326	1.466	±0.070	1.458	0.008	0.57
(4 2 0)	7.317	0.378	1.366	±0.071	1.304	0.062	4.76

Table S2: Measured and reference interplanar spacings for encapsulated β-Sn nanowire viewed down the tetragonal [010] zone axis.

assigned plane	FFT freq. (nm^{-1})	FFT ± Δfreq. (nm^{-1})	measured d (Å)	± Δd (Å)	literature d (Å)	Δd (Å) = meas – lit	deviation (%)
(3 0 1)	3.595	0.35	2.782	±0.27	2.794	−0.012	-0.43
(2 0 0)	3.468	0.35	2.883	±0.29	2.945	−0.062	-2.11

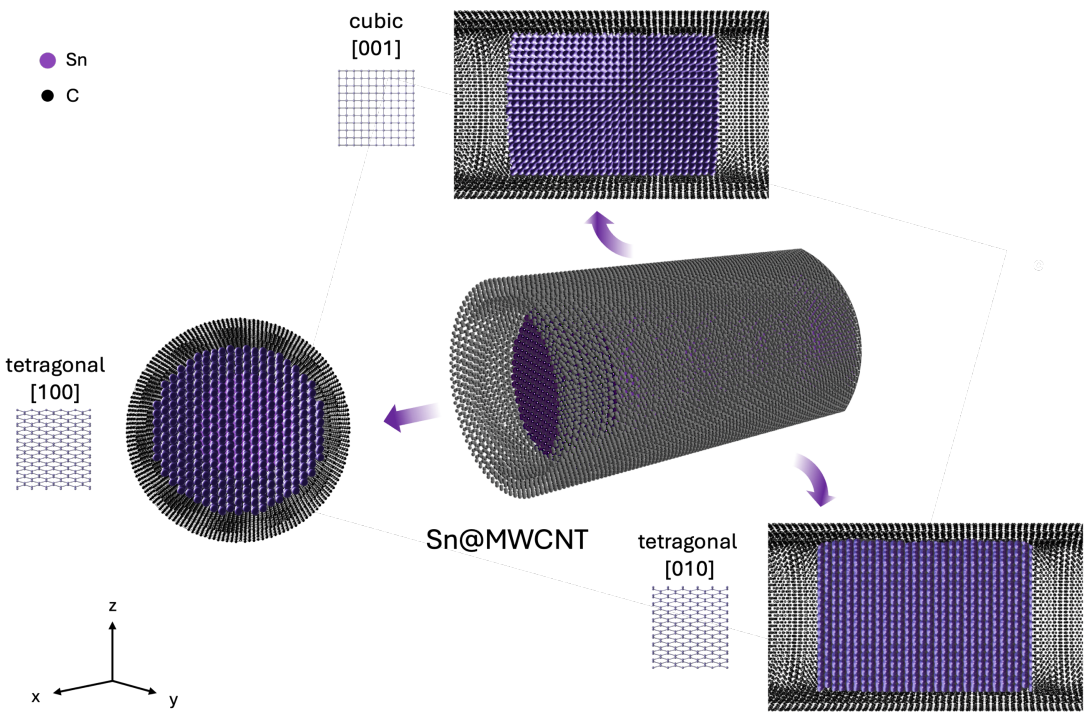

Fig. S1: Orientation analysis of two encapsulated Sn nanowires. *Schematic illustration showing the crystallographic orientation and spatial configuration of two single-crystal β-Sn nanowires confined within a MWCNT. The cubic [001] and tetragonal [010] faces are observed in contact with the inner walls of the nanotube, while the tetragonal [100] face lies along the nanotube axis. This configuration highlights the orthogonal relationship between crystal facets and the cylindrical confinement. Face assignment was based on the observed faceting at the interface between the nanowire and the CNT wall, indicating that both nanowires are oriented with the [001] and [010] faces facing the wall, and the [100] face directed along the axial channel of the nanotube. The inner diameter of the MWCNT is 3 nm.*

2. Disproportionation behaviour of SnO

The amorphous character of the encapsulated material inside the nanotube arises from the complex thermochemistry of SnO, which undergoes multi-step disproportionation involving intermediate oxidation states. This transformation can be broadly represented as:

$$2\mathrm{SnO}_{(s)} \rightarrow \text{intermediate } \mathrm{Sn_xO}_{(g)} \rightarrow \mathrm{Sn}_{(s)} + \mathrm{SnO_{2\,(s)}}$$

where the intermediate vapour-phase species (Sn_xO) may include mixed-valence compounds, such as Sn_2O_3 and Sn_3O_4 – both of which were observed as transient crystalline domains *in situ*, see Supplementary Section 5. The formation and decomposition of these intermediates are governed by the local oxygen chemical potential and vapour saturation within the confined nanotube environment. This dynamic evolution of phases disrupts long-range crystallinity, producing an amorphous matrix interspersed with Sn-rich and Sn-poor regions. The resulting heterogeneity reflects the reactive nature of SnO disproportionation and its role in driving the encapsulation process under confinement.

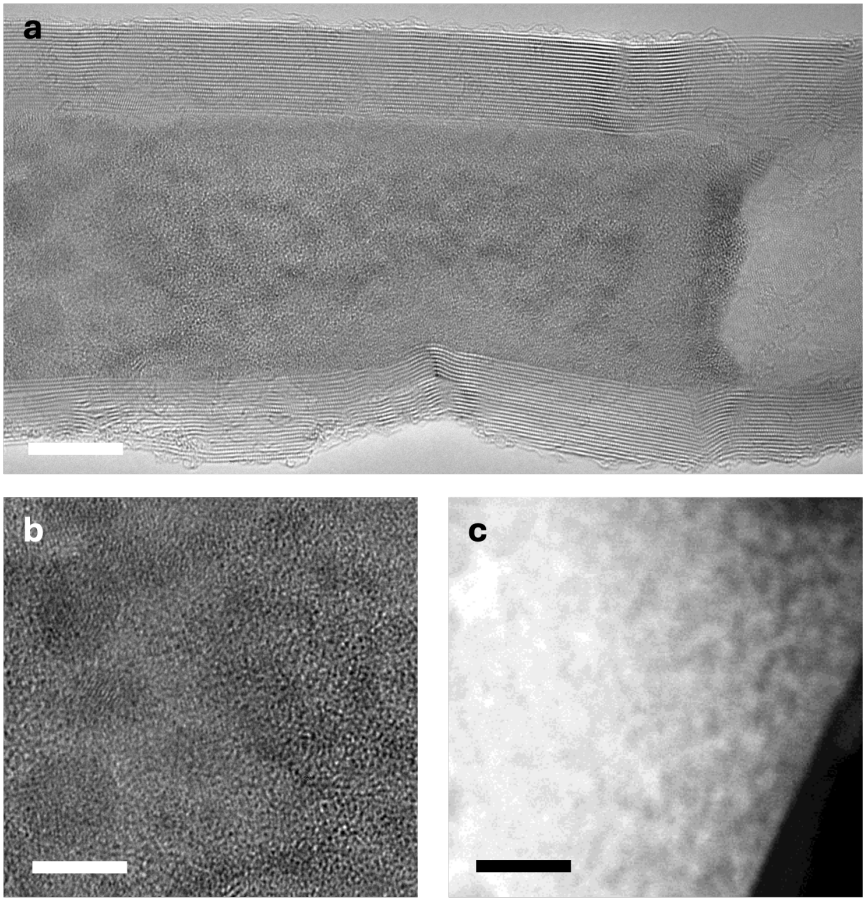

Fig. S2: ARTEM image of disproportionation of SnO within the nanotube core. a*, BF-ARTEM micrograph showing a SnO-filled MWCNT.* ***b****, High-magnification ARTEM micrograph highlighting the amorphous morphology of the encapsulated SnO nanowire, showing the local disproportionation, with dark contrasting regions corresponding to metallic Sn embedded within*

an amorphous oxide matrix. ***c****, Angular dark-field scanning TEM (ADF-STEM) micrograph of a similar region, complementing the bright-field ARTEM micrograph, showing chemical contrast with the bright metallic Sn domains embedded within the oxide matrix, providing insight into local disproportionation upon cooling. Scale bars:* ***a****, 10nm,* ***b****, 4 nm, and* ***c****, 5 nm.*

A representative bright-field ARTEM micrograph and annular dark-field scanning transmission electron microscopy (ADF-STEM) image (Figure S2) reveal an amorphous, oxygen-rich SnO domain encapsulated within the central cavity of a MWCNT. Embedded within this matrix are nanocrystalline domains ranging from 1–4 nm, displaying heterogeneous contrast in both imaging modes. This variation likely reflects local Sn enrichment, as regions with higher atomic number (Z) scatter electrons more strongly, producing brighter or darker features depending on the imaging conditions.

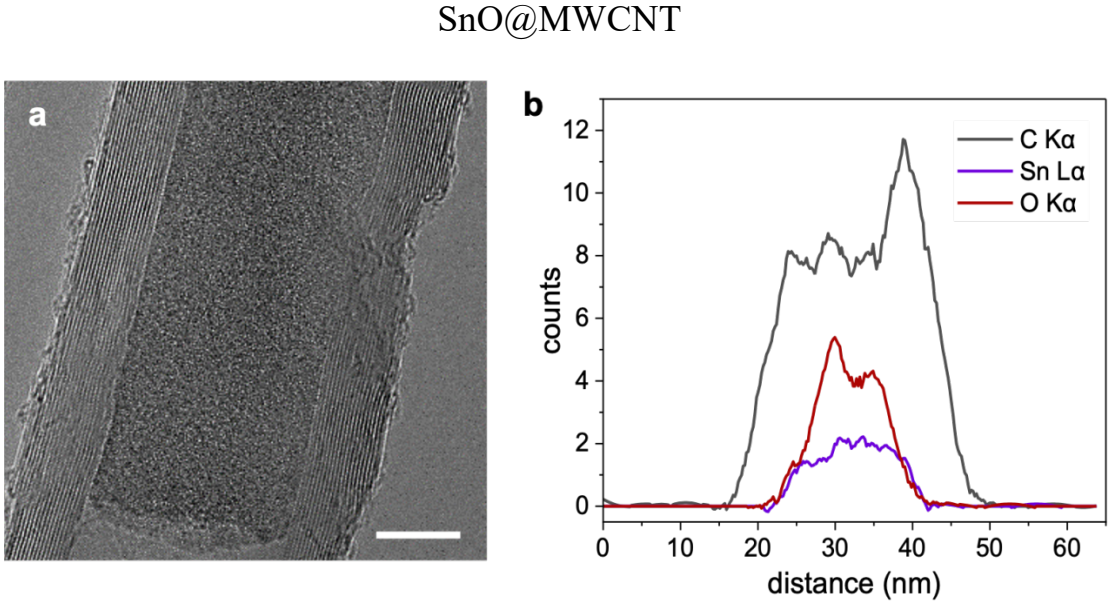

Fig. S3: Energy dispersive spectroscopy (EDS) to confirm the encapsulation of a SnO within MWCNT*.* ***a****, BF-ARTEM micrograph of SnO-filled MWCNT (SnO@MWCNT).* ***b****, EDS line profile across the SnO-filled nanotube, showing spatially resolved Sn and O signals confined to the inner core, confirming the axial encapsulation of SnO. EDS measurements were performed at 80 kV under beam-sensitive conditions.*

To confirm the composition of the encapsulated phase, elemental analysis was conducted using Energy-Dispersive X-ray Spectroscopy (EDS) line scans across the MWCNT. The simultaneous presence of Sn and O peaks, spatially centred within the carbon shell, confirms the axial confinement of SnO within the nanotube.

3. Convolution Neural Network (CNN) micrograph processing:

To automate the pixel-wise classification of high-resolution ARTEM micrographs, we developed a CNN-based micrograph processing pipeline that preserves atomic-scale details. Our workflow encompasses micrograph acquisition, manual labelling for CNN training, and pixel-level classification, ensuring that the original resolution and precise atom placements are maintained throughout processing. The following sections describe the complete workflow in detail.

Micrograph training

Depending on the experiment, between 19 and 22 training micrographs were collected, with a micrograph size ranging from approximately 1500×2500 to 2500×5000 pixels. The micrographs were stored as 8-bit grayscale TIFF files to avoid compression artefacts. Each training micrograph was manually annotated at the pixel level to label seven distinct atomic features: MWCNT wall, empty tube, amorphous SnO, liquid SnO, Sn_2O_3 (metallic oxide), Sn_3O_4, and background. The micrographs were cropped to predominantly include the MWCNT region and rotated so that the nanotubes were vertically aligned. Figure 1 shows a sample nanotube micrograph along with its corresponding expert annotations, with different colours representing the various regions. During acquisition, care was taken to ensure that each pixel area corresponded to the same physical area across all micrograph samples.

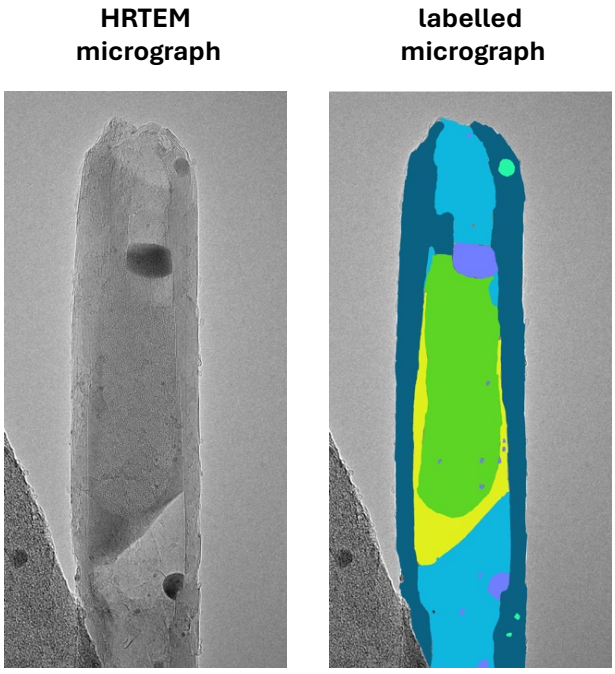

Figure 1: ARTEM micrograph labelling. *Example of micrograph labelling for CNN training: the left panel shows an original ARTEM micrograph, and the right panel displays the corresponding annotated regions.*

Model

Due to the limited number of micrographs and their extreme spatial resolution, which pose computational challenges for pixel-wise region classification, a CNN patch filter was implemented. Specifically, the CNN was trained to classify each pixel based on the surrounding micrograph patch of size 64×64 pixels. In TEM micrographs, where key features such as atomic columns, lattice fringes, and phase boundaries often span only a few pixels, this loss proved detrimental. In contrast, our patch-based CNN performs pixel-wise classification directly at the full resolution without

interpolation, ensuring that fine details essential for accurate morphological and defect analysis are retained. This approach is particularly beneficial for dynamic *in situ* studies where transient and localized phenomena, such as single atom movement, may only be evident when observed at the native resolution.

The neural network employed in this study is a convolutional encoder with skip connections to classify pixels to region types based on input patches. The network architecture (Figure 2) comprised four residual blocks, each followed by a max-pooling layer for downsampling. Each residual block contained two convolutional layers and a skip connection. A single convolutional layer preceded the first residual block, while two dense layers followed the last, with sizes of 256 and N (where N represents the number of considered nanotube region types). All convolutions used 64 filters of size 3 x 3 pixels, and Leaky ReLU activation was applied after each convolutional layer. Finally, a softmax activation function was used to generate class probabilities.

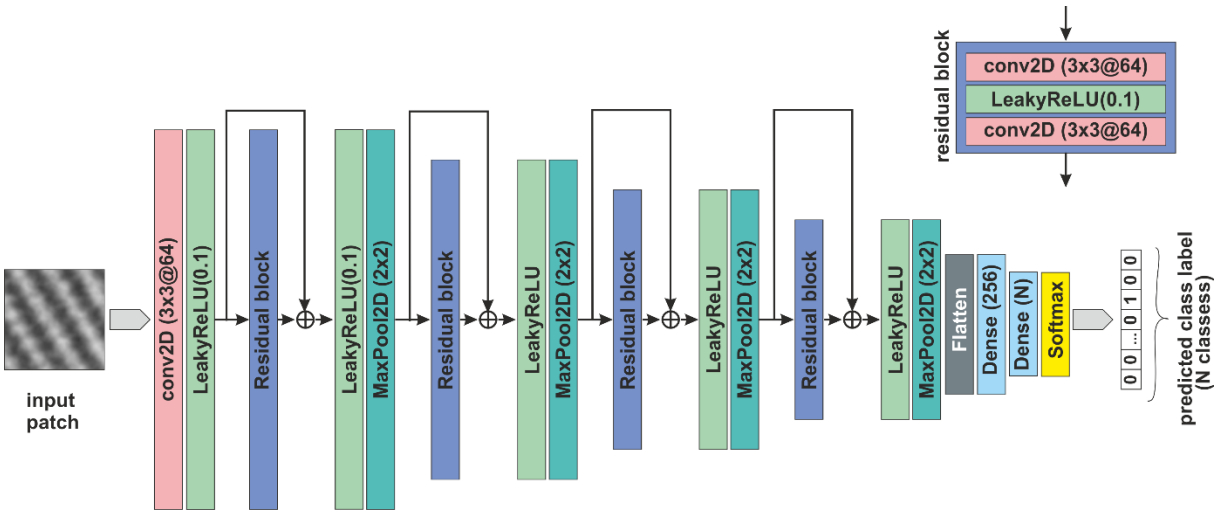

Figure 2: Schematic of the CNN architecture employed. *The network accepts a 64×64 input patch, passes it through an initial 3×3 convolutional layer (64 filters), and then through multiple residual blocks with LeakyReLU activations. The final layer is a fully connected layer for classification.*

Patches extraction for training

The CNN model was trained on 64 × 64 pixel patches extracted from ARTEM micrographs. Patches were systematically sampled row-by-row and column-by-column with a 10-pixel stride, ensuring that each patch contained at least one labelled pixel to reduce the prevalence of background regions. This approach generated approximately 35,000 to 120,000 training patches per micrograph, depending on the specific experiment and micrograph resolution. Each patch was assigned a region label based on the central pixel, capturing local structural features for robust feature learning. Prior to training, micrograph intensities were normalized to the range [0, 1] by dividing pixel values by 255 to standardize input contrast. The dataset was split into training (80%) and validation (20%) subsets to assess model performance. Representative examples of the extracted patches, covering the range of considered region types, are shown in Figure 3.

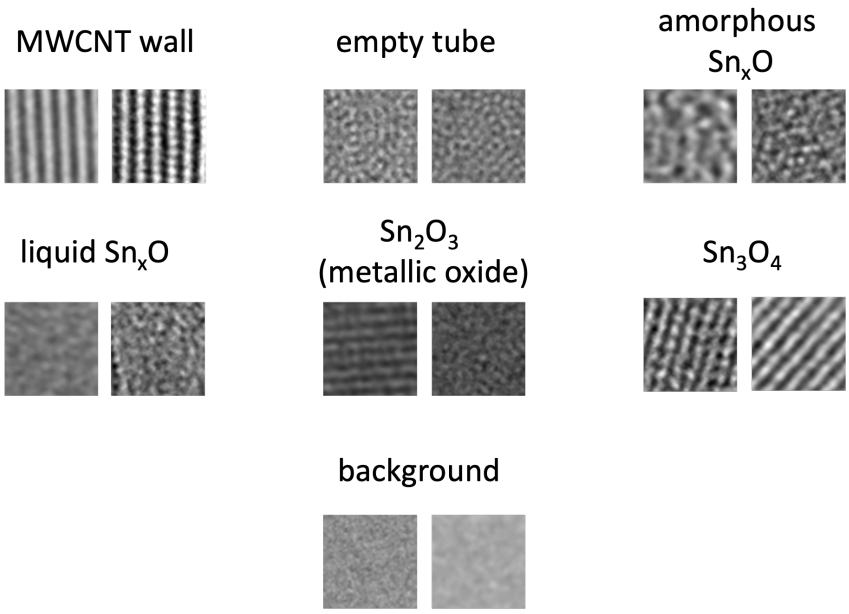

Figure 3: Representative Training Patches for Pixel Classification. *Examples of sample training patches (64 x 64 pixels) representing considered regions across the seven class types.*

Model training

The convolutional neural network was trained for 200 epochs using a mini-batch size of 4096. The Adam optimizer, configured with an initial learning rate of 0.001 and a decay rate of 0.001, was employed to minimize the cross-entropy loss. Early stopping was applied with a patience of 20 epochs, halting training after 20 consecutive epochs without improvement in the validation loss. The model weights corresponding to the lowest validation loss were then selected for inference. All training was performed on an NVIDIA Quadro RTX 6000 GPU.

Handling micrograph variance in ARTEM training

ARTEM micrographs exhibit significant contrast variance, as the micrograph intensity depends on the interference of electron waves that pass through and exit the sample. This phase contrast is highly sensitive to experimental conditions such as defocus, sample thickness, and beam brightness, leading to variations in the appearance of atomic features. This contrast is highly sensitive to experimental TEM parameters, including defocus, beam brightness, and sample thickness, all of which can alter the appearance of atomic-scale features (either as bright or dark contrast). These factors introduce artefacts that introduce variance in feature extraction and complicate classification in CNN recognition.

To address this, our CNN model was trained on a diverse set of 64 × 64 pixel patches extracted from micrographs collected under varying experimental conditions. This patch-based approach not only captures localized structural information but also reduces the influence of global contrast shifts, beam intensity fluctuations, and thickness variations. By exposing the model to a wide range of imaging conditions, we ensure that it learns to identify physically meaningful structures, improving classification accuracy and robustness against noise and artefacts. This strategy broadens the generalization of the model to new, unseen data, to capture the underlying atomic features of the patches.

Pixel classification

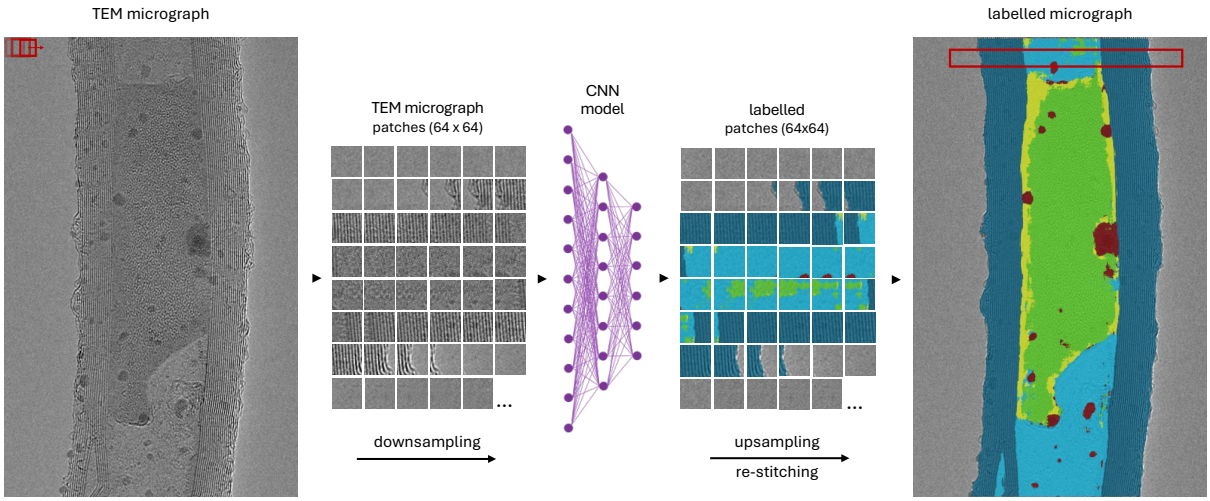

Figure 4: Patch-based segmentation strategy used to annotate the TEM micrographs whilst reattaining the original resolution of the micrograph. *The framework is based on the segmentation of the micrograph into numerous 64 x 64 pixel patches, where the central pixel is assigned by processing the patch through the pre-trained CNN model, and re-stitched through upsampling and overlaying of the patches to construct the fully annotated TEM micrograph.*

The trained CNN was used to classify consecutive pixels in unseen TEM micrograph. A sliding window approach was employed, where a patch-sized window was moved across the micrograph row-by-row and column-by-column. The framework of the patch-based strategy is shown in Figure 4 by the rastering of a 64 x 64 pixel patch across the micrograph that are classified through the model and reconstructed into a complete micrograph whilst retaining the spatial classification. Patches were sampled with a stride of 1, and the predicted label for each patch was assigned to its centre pixel. This process produced a continuous region-label map, where labels were assigned to every pixel in the micrograph.

4. *In situ* ARTEM and CNN processed micrographs:

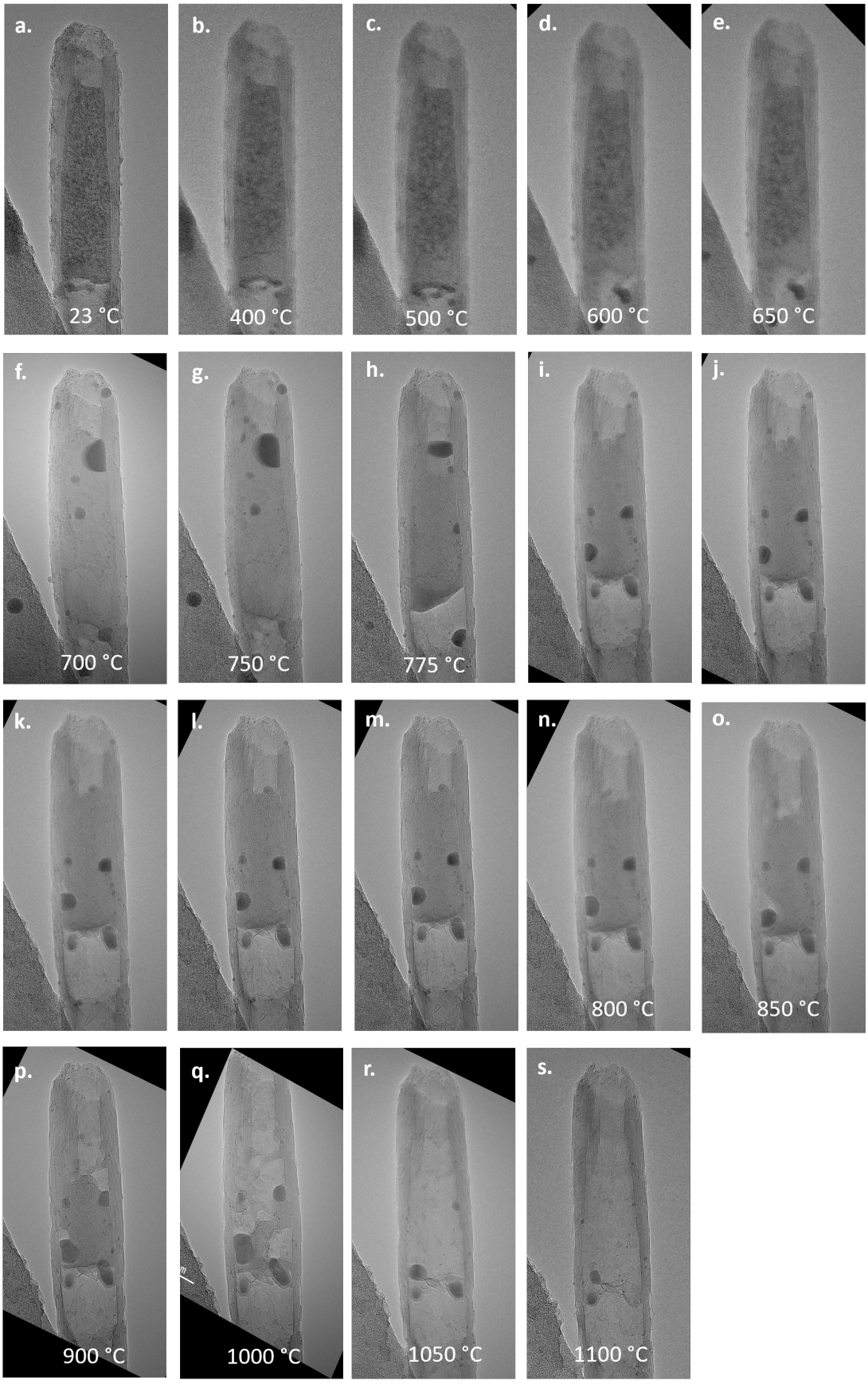

Fig. S4: Unprocessed in situ BF-ARTEM micrographs of a second encapsulated Sn_3O_4 nanowire encapsulated within a MWCNT. *All micrographs were captured at 80 kV.* ***a,*** *under static conditions at 23 °C,* ***b,*** *400 °C,* ***c,*** *500 °C,* ***d,*** *600 °C,* ***e,*** *650 °C,* ***f,*** *700 °C,* ***g,*** *750 °C,* ***h – m,*** *775 °C,* ***n,*** *800 °C,* ***o,*** *850 °C,* ***p,*** *900 °C,* ***q,*** *1000 °C,* ***r,*** *1050 °C,* ***s,*** *1100 °C.*

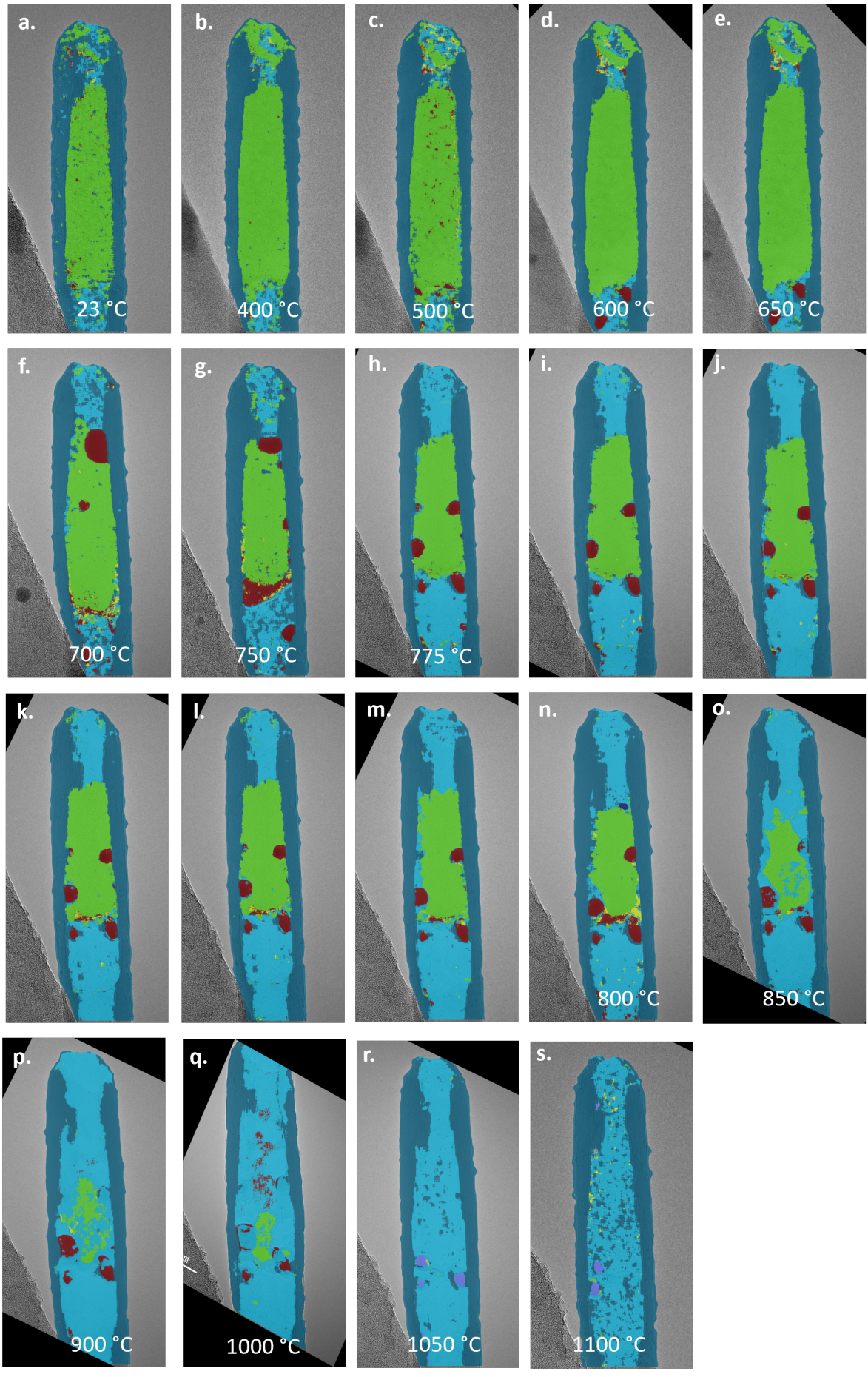
a.
23 °C
b.
400 °C
c.
500 °C
d.
600 °C
e.
650 °C
f.
700 °C
g.
750 °C
h.
775 °C
i.
j.
k.
l.
m.
n.
800 °C
o.
850 °C
p.
900 °C
q.
1000 °C
r.
1050 °C
s.
1100 °C

Fig. S5: Corresponding CNN-labelled micrographs of the second encapsulated Sn_3O_4 nanowire encapsulated within a MWCNT. a, *under static conditions at 23 °C,* ***b,*** *400 °C,* ***c,*** *500 °C,* ***d,*** *600 °C,* ***e,*** *650 °C,* ***f,*** *700 °C,* ***g,*** *750 °C,* ***h–m,*** *775 °C,* ***n,*** *800 °C,* ***o,*** *850 °C,* ***p,*** *900 °C,* ***q,*** *1000 °C,* ***r,*** *1050 °C,* ***s,*** *1100 °C. Colour-coded labels indicate textural classes identified by the CNN: dark blue (MWCNT wall), light blue (empty MWCNT core), green (amorphous Sn_xO), dark red (metallic Sn_2O_3), and yellow (liquid-phase Sn_xO).*

5. *In situ* formation of Sn_3O_4 and Sn_2O_3:

In situ observations reveal that intermediate SnO nanowires form during the early stages of vaporisation, subsequently undergoing disproportionation into transient mixed-valence phases such as Sn_2O_3 and Sn_3O_4 phases within the confined nanotube core, at various temperatures. These intermediates emerge at elevated temperatures and are likely derived from vapour-phase species, reflecting the complex phase evolution under confinement.

Triclinic Sn_2O_3 at 600 °C

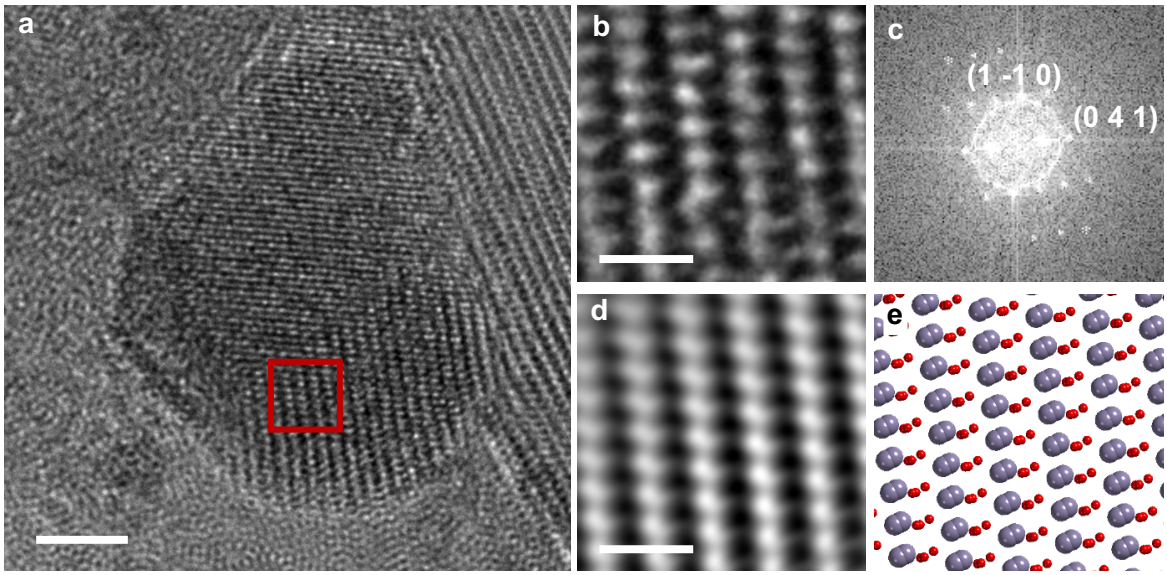

Fig. S6: in situ formation of intermediate Sn_2O_3 oxide imaged at 600℃. ***a****, BF-ARTEM micrograph providing an overview of the Sn_2O_3 crystal that formed at the carbon surface.* ***b****, A high-resolution image captures the atomic structure along the [-1 1 5] zone axis, where linear columns of bright contrast corresponding to Sn atoms are visible.* ***c****, The FFT reveals distinct spatial frequencies corresponding to the (1 -4 1) and (1 1 0) planes of Sn_2O_3.* ***d****, An inverse-FFT reconstructs the real-space atomic distribution, further confirming lattice periodicity.* ***e****, simulated [-1 1 5] face viewed under ARTEM. Scale bar:* ***a****, 2 nm,* ***b****, 0.7 nm,* ***c****, 5 nm^{-1}* ***d****, 0.7 nm.*

The crystal structure of Sn_2O_3 was identified by analysing the orientation and atomic arrangement in the ARTEM images. Using experimental X-ray diffraction data from literature[32], the unit cell was modelled with parameters: a = 3.710 Å, b = 8.180 Å, c = 5.460 Å; $\alpha = 90.000°$, $\beta = 92.300°$, and $\gamma = 93.800°$. Simulations were conducted using CrystalMaker to calculate d-spacings and generate atomic projections along the [1 1 −4] zone axis. A comparison between the experimentally measured and simulated d-spacings (Table S3) confirms the identification of the triclinic Sn_2O_3 phase. The slight deviation from ideal lattice vectors suggests a distorted superlattice structure, consistent with the observed metallic contrast and crystallographic distortions.

Table S3: Assigned planes and measured d-spacings of the Sn_2O_3 intermediate oxide observed in Figure S10 imaged at 600 ºC.

assigned plane	FFT freq. (nm^{-1})	FFT ± Δfreq. (nm^{-1})	measured d (Å)	± Δd (Å)	literature d (Å)	Δd (Å) = meas – lit	deviation (%)
(1 -4 1)	5.79	0.44	1.73	0.013	1.733	-0.003	-0.17
(1 1 0)	3.03	0.46	3.30	0.050	3.288	0.012	0.36

Throughout the *in situ* heating series, triclinic Sn_2O_3 phases were consistently with clearly resolved lattice fringes from 600-900°C. Similarly, Figure S9 presents a structural analysis of a triclinic Sn_2O_3 phase observed at 900 °C, further supporting the presence of this phase at elevated temperatures. A corresponding comparison of measured and simulated lattice spacings (Table S4).

Triclinic Sn_2O_3 at 900 °C

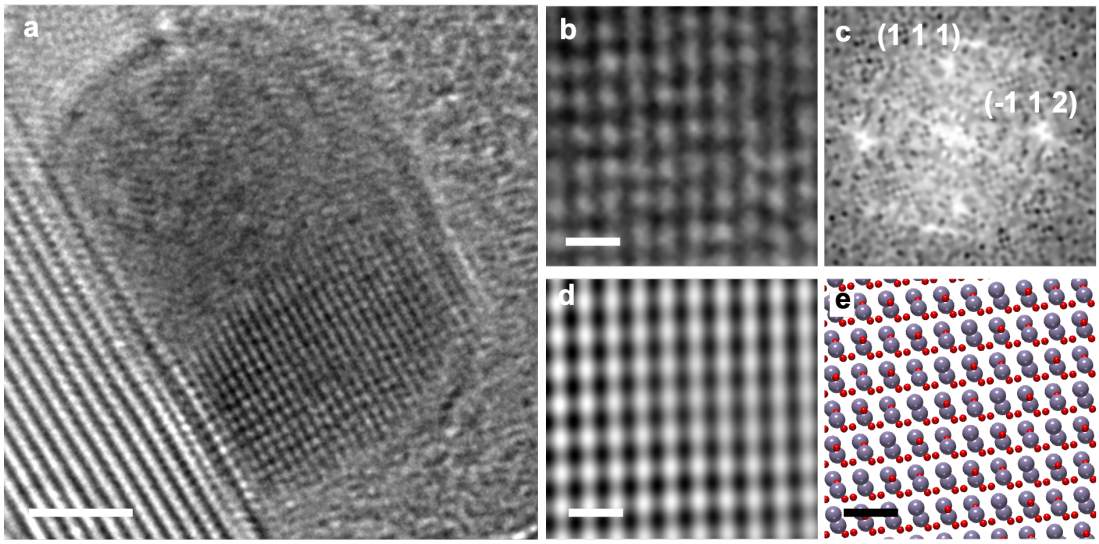

***Fig. S7: Structure of the triclinic Sn_2O_3 crystal imaged at 900 °C. a**, Low-magnification ARTEM micrograph of Sn_2O_3 crystal structure. **b**, High-magnification ARTEM micrograph imaged down the atomic columns of Sn_2O_3, **c**, FFT indicating the spatial distribution of periodic array, **d**, inverse-FFT of the isolate spatial frequencies that reveal the atomic array of the [1 -3 2] face. e, simulated projection of the [1 -3 2] face for comparison.*

Table S4: Measured and calculated *d*-spacings used for plane assignments for triclinic Sn_2O_3 at 900°C.

assigned plane	FFT freq. (nm^{-1})	FFT ± Δfreq. (nm^{-1})	measured d (Å)	± Δd (Å)	literature d (Å)	Δd (Å) = meas – lit	deviation (%)
(1 1 1)	7.28	0.46	2.79	0.087	2.77	-0.03	-1.08
(-1 1 2)	9.17	0.46	2.18	0.058	2.18	0.00	0.00

Sn_3O_4 at 750 °C

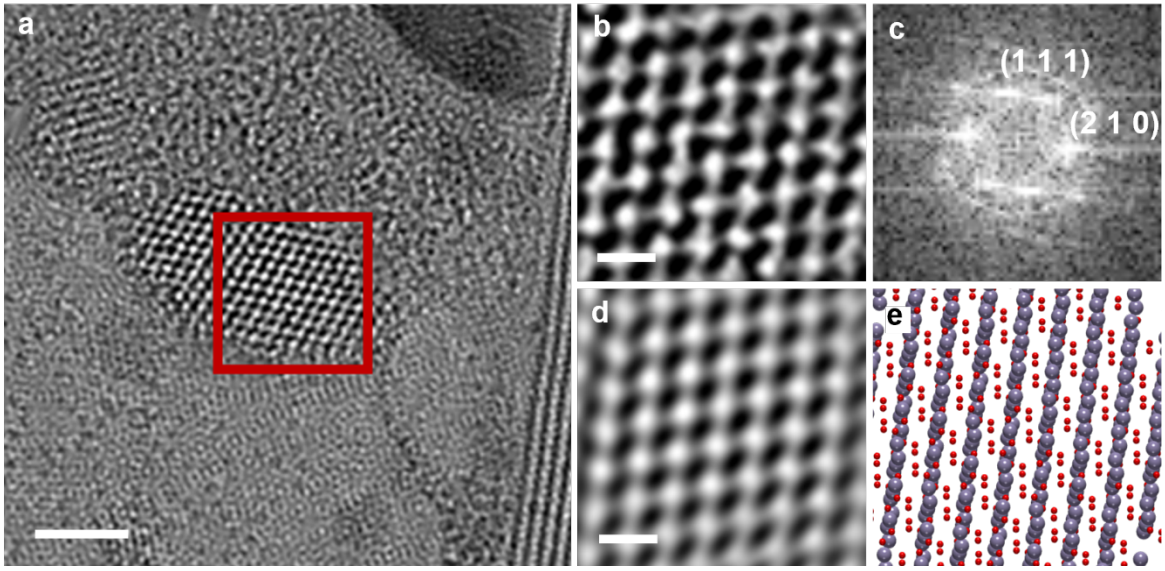

Fig. S8: Direct crystallographic evidence of Sn_3O_4 speciation. **a**, Overview ARTEM micrograph showing the Sn_3O_4 crystal structure at the liquid interface, recorded at 750°C. **b**, ARTEM micrograph of the Sn_3O_4 [-1 2 -1] zone axis, **c**, FFT displaying the spatial distribution corresponding to the (111) and (210) planes. **d**, inverse-FFT reconstructed using the (111) and (210) spatial frequencies, used to map the atomic positions. **e**, Simulated Sn_3O_4 structure oriented to the [-1 2 -1] face, illustrating the alignment of Sn atomic columns and interstitial positioning of oxygen atoms. Scale bar: **a**, 3 nm, **b**, 0.5 nm **d**, 0.5 nm.

During the *in situ* vaporisation of the SnO nanowire, Figure S11 shows the formation of an Sn_3O_4 crystal at 750 °C at the liquid-vapour interface. This short-lived intermediate, which vaporises within a few frames, is consistent with the monoclinic $P2_1/c$ structure, representing a distorted superlattice variant of cassiterite SnO_2 as reported[33]. The measured d-spacings and corresponding crystal planes for this Sn_3O_4 intermediate, extracted from FFT analysis, are presented in Table S5.

Table S5: Assigned planes and measured d-spacings of the Sn_3O_4 intermediate oxide observed in Figure S11 imaged at 750 °C.

assigned plane	FFT freq. (nm^{-1})	FFT ± Δfreq. (nm^{-1})	measured d (Å)	± Δd (Å)	literature d (Å)	Δd (Å) = meas – lit	deviation (%)
(1 -4 1)	5.79	0.44	1.73	0.013	1.733	-0.003	-0.17
(1 1 0)	3.03	0.46	3.30	0.050	3.288	0.012	0.36

6. Electron Energy Loss (EELS) Analysis

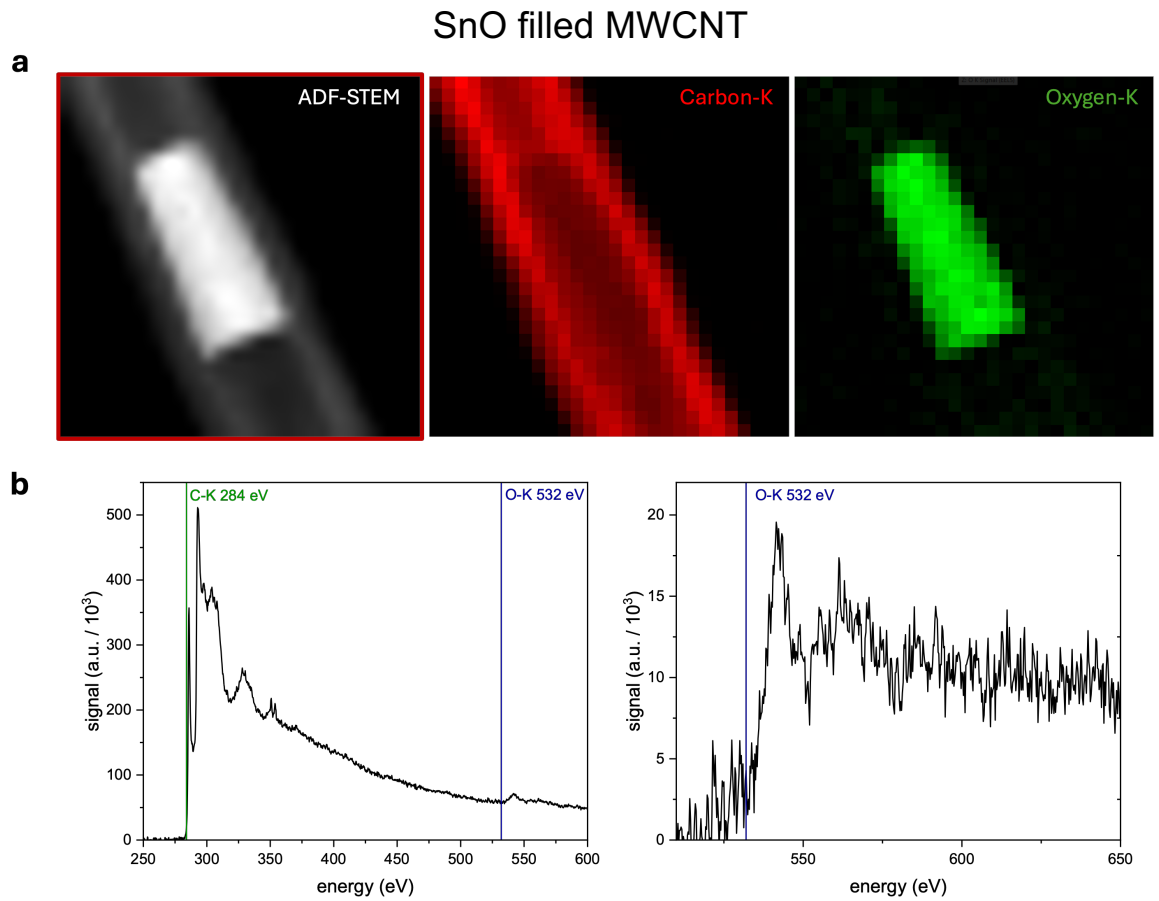

Figure S9: Structural and compositional analysis of SnO nanowire encapsulated within a MWCNT. a *ADF-STEM micrograph of the SnO nanowire encapsulated within the MWCNT, with corresponding elemental maps showing carbon (C-K, red) indicating the CNT structure and oxygen (O-K, green) indicating the SnO region.* ***b****, Electron energy loss spectra (EELS) from the same region, showing the low-loss spectrum for the carbon K-edge (284 eV) and the high-loss spectrum for the oxygen K-edge (532 eV), confirming the presence of both carbon and oxygen.*

The EELS spectrum was acquired by rastering the electron beam across the sample containing both unfilled MWCNTs and SnO-filled nanowires (as indicated by the red square surrounding the ADF-STEM micrograph). The resulting oxygen K-edge at 532 eV shows a clear correlation with the spatial distribution of the encapsulated SnO nanowire within the MWCNT core. The localized distribution of the oxygen-K edge signal, contrasts with the continuous wetting layer that would be expected if classical vapour condensation mechanisms.

The Sn M_4 (493 eV) and M_5 (485 eV) edges exhibit weak scattering cross-sections and overlap significantly with the O-K edge at 532 eV, as reported previously[34,35]. However, the presence of pre-edge features leading up to the oxygen K-edge provides indirect evidence for the presence of Sn, supporting the identification of encapsulated SnO within the nanotube cores. Reference spectra from the unfilled regions of the nanotube, as shown in Figure S14, confirm that the observed O-K edge is primarily associated with the spatial encapsulated SnO, rather than residual oxygen from acid oxidation of the MWCNT walls.

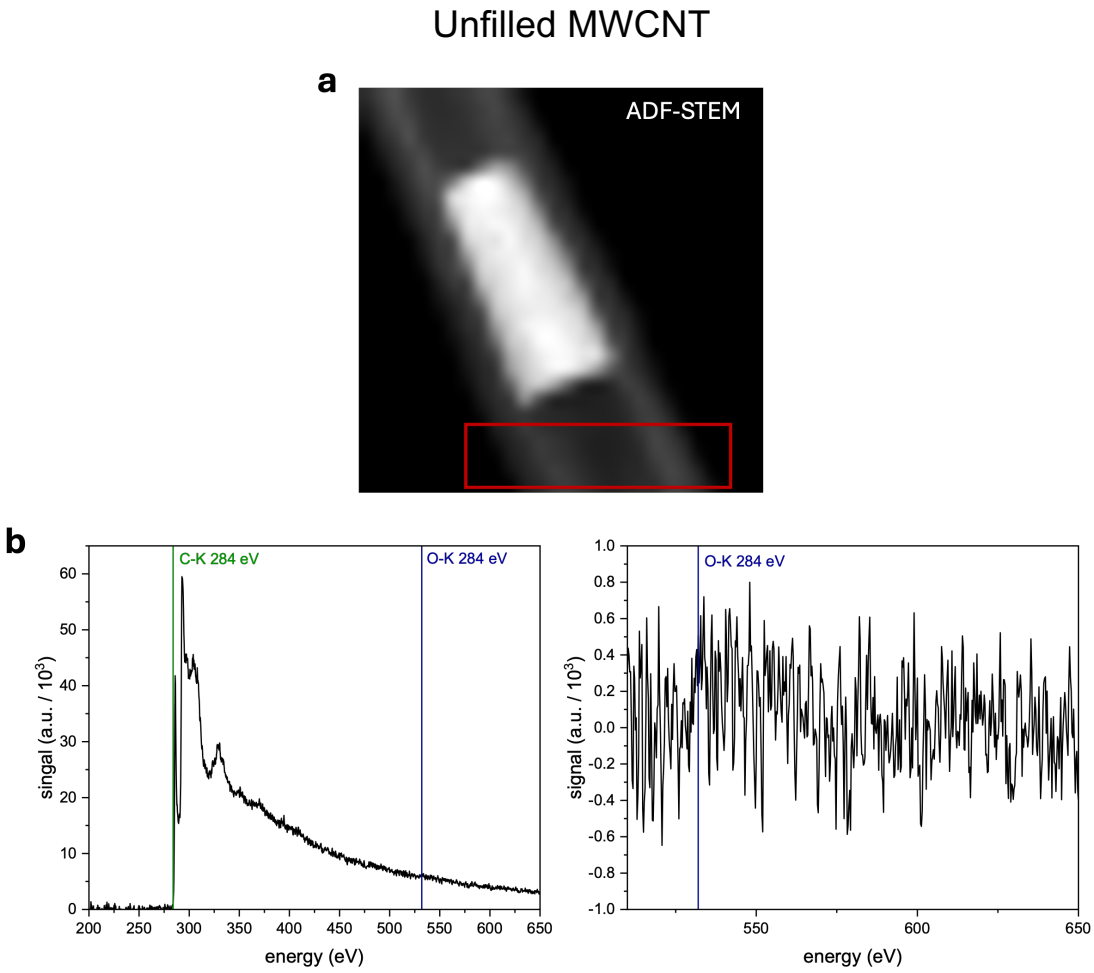

Fig. S10: EELS spectrum comparison of the unfilled oxygen edge. a*, the ADF-STEM micrograph highlights an unfilled section of the acid-treated MWCNT with a red region of interest selected to assess the possible contribution of oxygen from the unfilled MWCNT.* ***b****, the corresponding EELS spectra show a clear carbon K-edge (284 eV) without a significant oxygen K-edge (532 eV) signal, indicating that the observed oxygen in filled regions is primarily from the SnO encapsulated nanowire, rather than residual oxygen from the acid treatment of the nanotube.*

All EELS measurements were acquired as dual spectra to simultaneously capture high- and low- loss edges. The spectra were aligned to the zero-loss peak and background subtracted using a power-law fit to accurately isolate the core-loss edges.

7. Application of the Lucas–Washburn Model to Nanotube Filling Dynamics:

To investigate the growth dynamics of encapsulated SnO nanowires within MWCNTs, we applied the classical Lucas-Washburn (LW) model as a foundational framework for capillary-driven MWCNT filling. The LW model describes the capillary rise of a liquid into a cylindrical core of the tube, balancing the driving capillary pressure against, which drives the liquid flow, against the viscous drag, opposed the advancing meniscus.

The LW equation, derived from the Young-Laplace equation for capillary pressure and Poiseuille's law of viscosity, is given by:

$$L^2 = \frac{\gamma \cos\theta \, d}{4\eta} \cdot t$$

where, L is the length of the nanowire in the tube, γ is the liquid surface tension, θ is the liquid contact angle, η is the viscosity, t is time, and d is filled inner diameter.

The LW model provides a foundational framework for understanding the filling dynamics of SnO within MWCNTs by capturing the balance between capillary driving forces and viscous resistance, which are key factors governing material infiltration in nanoscale capillaries. From our observations, the advancing front of SnO within the MWCNT core is driven by capillary pressure and opposed by viscous drag, resembling the liquid meniscus dynamics described by the LW model. However, direct application of this model is limited due to the vapour-phase nature of SnO condensation within the MWCNT core, discrete nucleation events, and pronounced nanoscale effects influencing viscosity and contact angle. These complexities, coupled with the distribution of available MWCNT diameters, lead to varied filling rates and volumes, necessitating a generalized power-law model to describe the observed diameter dependent volume filling of different sized encapsulated SnO nanowires.

Deriving the power law filling model:

To capture these more complex dynamics, we extend the LW model to a power-law form where the filled volume depends on both the nanotube diameter and the exposed vapour annealing time, resulting in a power-law relation of:

$$V = ad^b$$

where, V is the filled volume, d is the diameter, α is the exponent factor reflecting the dimensional scaling, including effects from the dynamic contact angle and vapour flux and b is the scaling exponent.

The power law model emerges by combining the diameter dependent filling volume with the cylindrical volume of the tube:

$$V = d^2 L$$

where the volume, V, is equal to the nanotube cross-sectional area (d^2) and the filled length, L. According to the classical LW model, the filling length of a liquid in a tube scale with the

square root of time, reflecting the balance between capillary filling and opposing viscous forces:

$$L = \left(\frac{\gamma \cos\theta \, d}{4\eta} \cdot t\right)^{0.5}$$

For a given temperature series, parameters such as the surface tension, contact angle, and viscosity are assumed to remain constant at constant temperature for each annealing dataset. At a fixed annealing time, the filling length can be approximated to scale as:

$$L \propto d^{0.5}$$

Substituting this length scaling into the volume expression:

$$V \propto d^2 \cdot d^{0.5} = d^{2.5}$$

Equating to an overall power-law model of:

$$V = \alpha d^{2.5}$$

where the prefactor α captures the combined effects of surface tension, contact angle, viscosity, and temperature, as well as the dynamic interactions specific to the confined size of the MWCNT core.

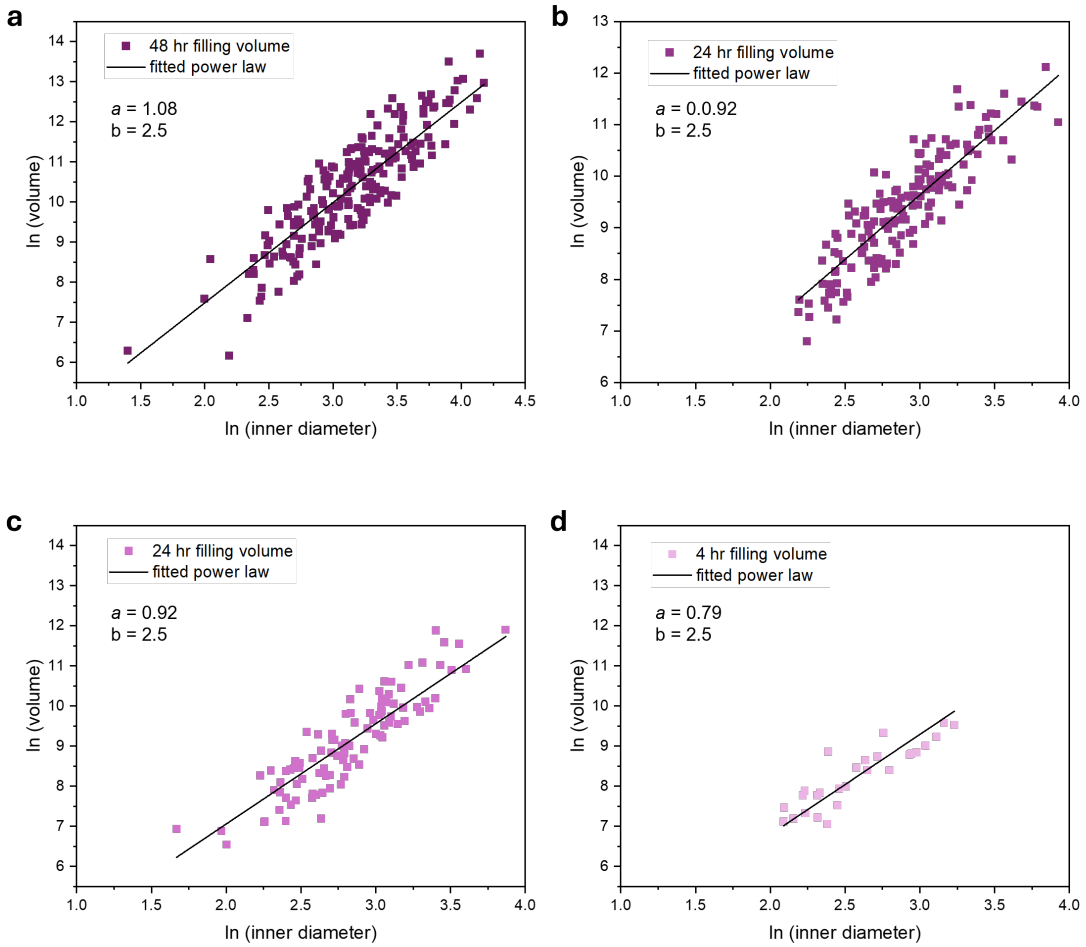

Fig. S11: Modelling the Encapsulated Nanowire Volume. *Linearised power-law scaling for SnO nanowire filling within MWCNTs at different annealing times.* ***a****, 48 h,* ***b****, 24 h,* ***c****, 24 h, and* ***d****, 4 h. Each plot shows the natural logarithm of filled volume versus the natural logarithm of inner diameter, with fitted power-law exponents consistently around b = 2.5, reflecting the combined effects of capillary-driven condensation and vapour-phase flux within the confined nanotube structure.*

The fitted power-law model ($V = ad^{2.5}$) was applied across different annealing times to analyse how the filling mechanism evolves. The extracted prefactor, a, and the R^2 coefficient values are summarized for each time series in Table S6.

Table S6: Fitted Power-Law Parameters for Each Annealing Time.

Annealing time (h)	prefactor (a)	R^2 coefficient
4	0.79	0.75
12	0.89	0.79
24	0.92	0.78
48	1.08	0.77

The gradual increase in the prefactor, a, from 0.79 at 4 h to 1.08 at 48 h indicates a progressive enhancement in overall filling efficiency for larger diameter nanotubes with greater annealing times.

In the early stages of filling, smaller-diameter nanotubes, which have lower nucleation barriers due to their higher curvature and reduced Kelvin radii, reach their condensation thresholds first. This initial nucleation locally depletes the surrounding vapour, effectively reducing the vapour pressure near these smaller tubes. As a result, the relative saturation near larger-diameter tubes increases with time to facilitate nanowire nucleation and growth. Consequently, the higher filling efficiency of larger nanotubes, which benefit from greater vapour flux and reduced viscous resistance, progressively enhances the collective growth rate, leading to larger nanowire volumes over time. The increasing filling rates of larger nanotubes over time are reflected in the rising prefactor, α, in each fitted power-law model, capturing the combined effects of enhanced vapour flux and reduced internal resistance, which together drive the efficient filling of larger-diameter nanotubes. The increased filling of larger-diameter nanotubes, which only become activated at longer annealing times due to their higher nucleation thresholds, indicates that the overall kinetic filling process is not limited by vapour flux.

The growth of nanowires within nanotubes is opposed by internal viscous drag, which becomes increasingly significant at the nanoscale due to the greater surface-to-volume interactions and confinement of the nanotube core. As the liquid meniscus advances within the confined nanotube core, this viscous resistance typically slows the filling rate, consistent with the classical Lucas-Washburn model and the observed b = 2.5 power-law scaling for volume filling over time. However, this drag is partially offset by the simultaneous rise in local vapour saturation, driven by the progressive depletion of smaller filled tubes. As the local vapour pressure increases, it sustains a net positive driving force for capillary flow within the MWCNT core, counteracting the increasing internal viscous drag that typically resists nanowire growth and promoting the formation of continuously encapsulated nanowires.

The moderately high R^2 values (0.75 to 0.80) observed across all time points indicate that the power-law model with a fixed exponent of b = 2.5 provides a reasonably good fit to the observed filling data, capturing the dominant trend of nanowire growth within the confined MWCNT structure.

For comparison, each annealing time series was fitted with the power-law ($V = \alpha d^b$), which allows both the prefactor (α) and the scaling exponent (b) to vary independently, fitted in Figure S12 and summarized in Table S7.

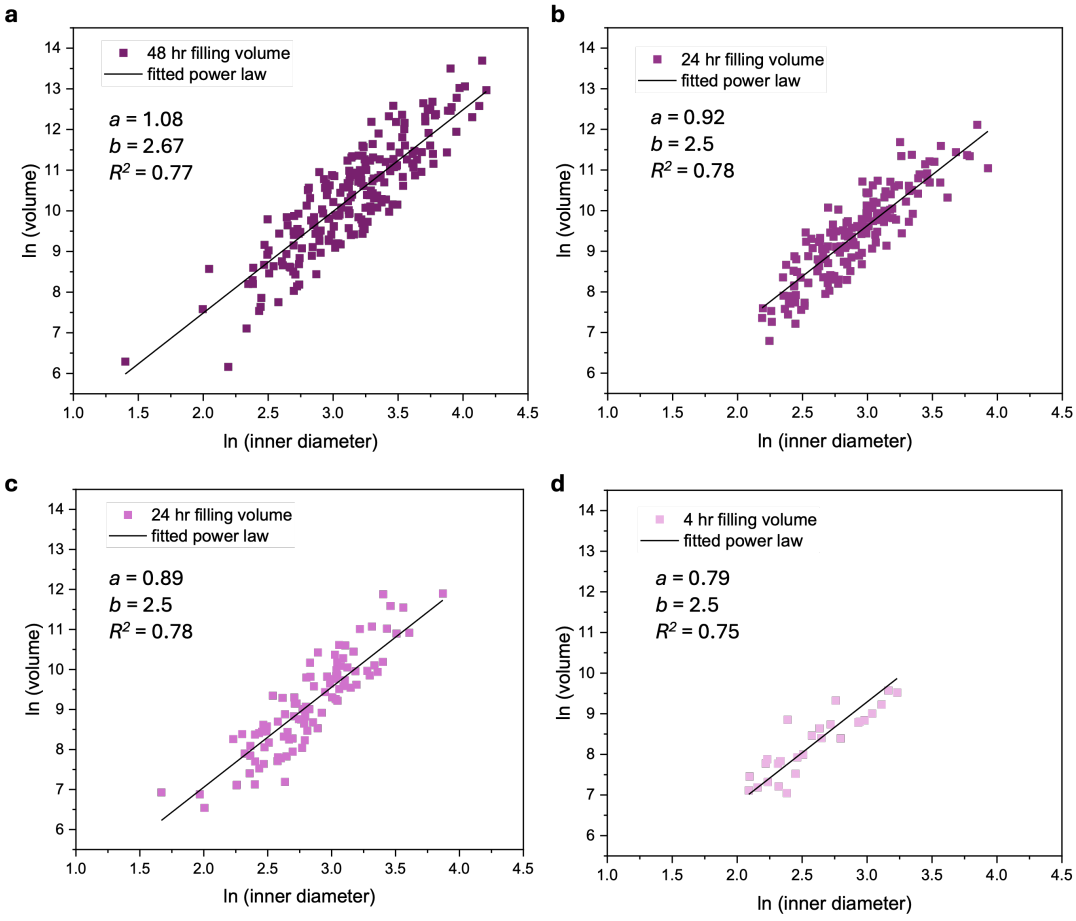

Figure S12: Modelling the volume of filling with unfixed fitting parameters. *Linearised power-law model to fit for both the prefactor (a) and exponent (b) for the volume of SnO-nanowire filled confined with MWCNTs.* ***a****, 48 h,* ***b****, 24 h,* ***c****, 12 h,* ***d****, 4 h. Each plot is fitted with the nature natural logarithm of filled volume (V) versus the natural logarithm inner diameter (d) fitted with a liner regression.*

Table S7: Fitting Parameters for Non-Fixed Power-Law Model

Annealing time (h)	α	b	R^2 coefficient
4	0.79	2.21	0.76
12	0.89	2.76	0.80
24	0.92	2.63	0.78
48	1.08	2.67	0.77

8. Statistic growth dynamics

Table S8: Summary statistics for SnO-filled nanotube diameter, nanowire length, and aspect ratio with increasing annealing time. (All values displayed in nm units).

filled inner diameters									
annealing time (h)	**count**	**mean**	**std**	**min**	**25 %**	**50 %**	**75 %**	**max**	**IQR**
4	28	14.35	5.27	8.08	10.16	12.70	18.82	25.31	8.66
12	97	18.05	7.22	5.31	13.16	16.41	21.31	47.95	8.16
24	163	19.30	7.68	8.92	13.94	17.40	22.83	50.76	8.90
48	213	25.40	11.28	4.05	17.34	23.24	30.91	65.31	13.58

nanowire length									
annealing time (h)	**count**	**mean**	**std**	**min**	**25 %**	**50 %**	**75 %**	**max**	**IQR**
4	28	30.10	18.50	11.51	21.46	24.33	31.90	10.44	10.44
12	97	45.23	30.18	8.02	25.41	37.36	55.60	187.73	30.18
24	163	49.13	29.43	11.73	26.20	44.20	62.56	209.58	36.36
48	213	85.75	61.62	6.94	40.57	70.16	115.14	348.49	74.60

aspect ratio									
annealing time (h)	**count**	**mean**	**std**	**min**	**25 %**	**50 %**	**75 %**	**max**	**IQR**
4	28	2.28	1.28	0.99	1.17	2.06	2.72	6.35	1.54
12	97	2.60	1.50	0.58	1.48	2.25	3.23	8.02	1.76
24	163	2.68	1.50	0.56	1.60	2.27	3.19	8.54	1.59
48	213	3.61	2.45	0.77	1.73	2.89	4.65	13.43	2.92

9. References:

32. Mäki-Jaskari, M. A. & Rantala, T. T. Possible structures of nonstoichiometric tin oxide: the composition Sn_2O_3. *Model Simul Mat Sci Eng* **12**, 33–41 (2004).

33. White, T. A., Moreno, M. S. & Midgley, P. A. Structure determination of the intermediate tin oxide Sn_3O_4 by precession electron diffraction. *Zeitschrift für Kristallographie* **225**, 56–66 (2010).

34. Moreno, M. S., Egerton, R. F. & Midgley, P. A. Differentiation of tin oxides using electron energy-loss spectroscopy. *Phys Rev B* **69**, 233304 (2004).

35. Moreno, M. S., Egerton, R. F., Rehr, J. J. & Midgley, P. A. Electronic structure of tin oxides by electron energy loss spectroscopy and real-space multiple scattering calculations. *Phys Rev B* **71**, 035103 (2005).